The Planetary Science Journal, 3:96 (13pp), 2022 April https://doi.org/10.3847/PSJ/ac650f

Uranus's and Neptune's Stratospheric Water Abundance and Vertical Profile from Herschel-HIFI*

N. A. Teanby[1], P. G. J. Irwin[2], M. Sylvestre[1], C. A. Nixon[3], and M. A. Cordiner[3,4]
[1] School of Earth Sciences, University of Bristol, Wills Memorial Building, Queens Road, Bristol, BS8 1RJ, UK; n.teanby@bristol.ac.uk
[2] Atmospheric, Oceanic & Planetary Physics, Department of Physics, University of Oxford, Clarendon Laboratory, Parks Road, Oxford, OX1 3PU, UK
[3] Solar System Exploration Division, NASA Goddard Space Flight Center, 8800 Greenbelt Road, Greenbelt, MD 20771, USA
[4] Department of Physics, Catholic University of America, Washington, DC 20064, USA
Received 2021 September 17; revised 2022 April 4; accepted 2022 April 5; published 2022 April 29

Abstract

Here we present new constraints on Uranus's and Neptune's externally sourced stratospheric water abundance using disk-averaged observations of the 557 GHz emission line from Herschel's Heterodyne Instrument for the Far-Infrared. Derived stratospheric column water abundances are $0.54^{+0.26}_{-0.06} \times 10^{14}$ cm^{-2} for Uranus and $1.9^{+0.2}_{-0.3} \times 10^{14}$ cm^{-2} for Neptune, consistent with previous determinations using ISO-SWS and Herschel-PACS. For Uranus, excellent observational fits are obtained by scaling photochemical model profiles or with step-type profiles with water vapor limited to $\leqslant$0.6 mbar. However, Uranus's cold stratospheric temperatures imply a $\sim$0.03 mbar condensation level, which further limits water vapor to pressures $\leqslant$0.03 mbar. Neptune's warmer stratosphere has a deeper $\sim$1 mbar condensation level, so emission-line pressure broadening can be used to further constrain the water profile. For Neptune, excellent fits are obtained using step-type profiles with cutoffs of $\sim$0.3–0.6 mbar or by scaling a photochemical model profile. Step-type profiles with cutoffs $\geqslant$1.0 mbar or $\leqslant$0.1 mbar can be rejected with 4σ significance. Rescaling photochemical model profiles from Moses & Poppe to match our observed column abundances implies similar external water fluxes for both planets: $8.3^{+4.0}_{-0.9} \times 10^4$ cm^{-2} s^{-1} for Uranus and $12.7^{+1.3}_{-2.0} \times 10^4$ cm^{-2} s^{-1} for Neptune. This suggests that Neptune's $\sim$4 times greater observed water column abundance is primarily caused by its warmer stratosphere preventing loss by condensation, rather than by a significantly more intense external source. To reconcile these water fluxes with other stratospheric oxygen species (CO and CO_2) requires either a significant CO component in interplanetary dust particles (Uranus) or contributions from cometary impacts (Uranus, Neptune).

Unified Astronomy Thesaurus concepts: Neptune (1096); Uranus (1751); Planetary atmospheres (1244); Submillimeter astronomy (1647)

Supporting material: data behind figures

1. Introduction

Water in the stratospheres of ice giants Uranus and Neptune has previously been demonstrated to originate from external sources. These sources include comet impacts (Lellouch et al. 2005), interplanetary dust particles (Poppe 2016), or rings and moons (Cavalié et al. 2019). There are also large reservoirs of water in ice giant deep interiors (Luszcz-Cook & de Pater 2013; Cavalié et al. 2017; Atreya et al. 2020), but these are not expected to be a significant source of stratospheric water owing to the tropopause cold trap, with water ice clouds forming at pressures greater than 10 bars (Atreya et al. 2020). For example, at a typical ice giant tropopause temperature of $\sim$50 K (Lindal et al. 1987; Lindal 1992) the water saturation vapor pressure (SVP) is $\sim 10^{-40}$ Pa (Murphy & Koop 2005), far too low to allow significant amounts into the stratosphere. Measurements of water vapor abundance in Uranus's and Neptune's atmospheres thus provide important constraints on external flux processes and stratospheric chemistry (Moses et al. 2020).

Water abundance measurements on the ice giants are difficult from Earth-based observatories, due to the high abundance of water vapor in Earth's atmosphere. Therefore, measurements rely on space-based telescopes and spacecraft missions. Stratospheric water was first detected on Uranus and Neptune by the Short-Wavelength Spectrometer (SWS) on the Infrared Space Observatory (ISO; Feuchtgruber et al. 1997). For Uranus, Feuchtgruber et al. (1997) fitted the SWS spectrum with two types of profile: a uniform volume mixing ratio (VMR) profile with 5–12 ppb (parts per billion) water above the condensation level at 0.025–0.035 mbar, and a gradient profile with an external water flux of $(0.6–1.6) \times 10^5$ cm^{-2} s^{-1} combined with an assumed eddy mixing profile. For both profile types, Uranus's column water abundance was $(0.5–1.2) \times 10^{14}$ cm^{-2} (Feuchtgruber et al. 1997). For Neptune, Feuchtgruber et al. (1997) determined a water abundance of 1.5–3.5 ppb assuming a uniform VMR above the 0.55–0.70 mbar condensation level. They also fitted external source profiles assuming two different eddy mixing profiles that required an external water flux of $(1.2–150) \times 10^5$ cm^{-2} s^{-1}. Uncertainty in external flux was large owing to the large differences in assumed eddy mixing profiles and resulting VMR profiles (Feuchtgruber et al. 1997). Neptune's stratosphere is warmer than Uranus's (Lindal et al. 1987; Lindal 1992) and has a much deeper condensation level,

* Herschel is an ESA space observatory with science instruments provided by European-led Principal Investigator consortia and with important participation from NASA.

so that both mixing processes and ablation become important, and choice of profile has a greater influence on derived fluxes. However, water column abundance is more robust to profile assumptions and could be constrained to (2–6) $\times 10^{14}$ cm^{-2} for all profile types (Feuchtgruber et al. 1997). This demonstrates that Neptune has significantly more stratospheric water than Uranus, by a factor of ~2–4, perhaps suggesting a more intense external flux on Neptune.

Further constraints on Neptune's stratospheric water were obtained using Herschel's Photodetector Array Camera and Spectrometer (PACS; Lellouch et al. 2010). Lellouch et al. (2010) measured a column abundance of $(2.1 \pm 0.5) \times 10^{14}$ cm^{-2}, corresponding to a VMR of 0.85 ± 0.2 ppb for a uniform profile above a 1.2 mbar condensation level (a slightly higher pressure than in Feuchtgruber et al. 1997 due to a slightly warmer temperature profile being used in the analysis). External flux derived from these measurements again had a strong dependence on profile assumptions with a range of (1.4–90) $\times 10^5$ cm^{-2} s^{-1}. While the PACS instrument could not resolve water line shape, Lellouch et al. (2010) argue that observed integrated water line areas preferred an external source profile with VMR increasing for pressures below 0.1–1 mbar (their profile "A"). This favored an external flux closer to 1.4×10^5 cm^{-2} s^{-1}.

Therefore, previous measurements constrain water column abundance on Uranus and Neptune reasonably well, but VMR at a particular pressure level and inferred external fluxes have a strong dependence on profile assumptions.

Two other externally sourced oxygen species, CO and CO_2, have also been observed in ice giant stratospheres. On Uranus, CO has been measured in the stratosphere at 7.1–9.0 ppb assuming a uniform VMR profile above the tropopause (pressures less than 100 mbar; Cavalié et al. 2014). However, CO has not been observed in the troposphere yet, with an upper limit of <2.1 ppb for pressures greater than 100 mbar (Teanby & Irwin 2013), confirming stratospheric CO also has an external source. On Neptune, CO has a very high abundance of ~1 ppm (parts per million) in the stratosphere (Lellouch et al. 2005; Hesman et al. 2007; Luszcz-Cook & de Pater 2013; Teanby et al. 2019), much greater than on any other giant planet. There is also evidence that CO may exist in Neptune's troposphere with an abundance of ~0.1 ppm, which may require an additional internal source (Lellouch et al. 2005; Luszcz-Cook & de Pater 2013; Cavalié et al. 2017). However, this is somewhat controversial, as current observations can only probe the upper troposphere (Teanby et al. 2020). Stratospheric CO_2 has also been detected with column abundances of $(0.17 \pm 0.04) \times 10^{14}$ cm^{-2} on Uranus with Spitzer (Orton et al. 2014) and 8×10^{14} cm^{-2} on Neptune with ISO (Feuchtgruber et al. 1997).

Observations of stratospheric oxygen species H_2O, CO, and CO_2 in combination with photochemical models can be used to investigate external fluxes and source material properties. The most comprehensive study to date is by Moses & Poppe (2017), who use interplanetary dust particle (IDP) fluxes based on a dynamical model (Poppe 2016) coupled with a photochemical and ablation scheme to predict stratospheric abundances for all four giant planets. The ablation model predicts an oxygen atom flux of $8.9^{+19}_{-6.1} \times 10^4$ cm^{-2} s^{-1} for Uranus and $7.5^{+16}_{-5.1} \times 10^5$ cm^{-2} s^{-1} for Neptune. The resulting match to observed CO, CO_2, and H_2O abundances depends on ice grain composition, atmospheric composition, and subsequent chemistry. Atmospheric chemistry and the resulting balance of oxygen species abundance differ somewhat on Uranus and Neptune owing to the much lower altitude of Uranus's CH_4 homopause and the presence of CH_4 higher up in Neptune's atmosphere.

For Uranus, a reasonable match of model predictions to available H_2O, CO, and CO_2 observations is possible. However, O atom influx has to be increased to 4×10^5 cm^{-2} s^{-1}, slightly above the upper end of model estimates, and IDP grains require a significant fraction of CO (69% CO, 31% H_2O, and 0.8% CO_2; Moses & Poppe 2017). Alternatively, the higher-than-predicted flux may suggest a cometary CO and CO_2 contribution in the past few hundred years. Relatively high stratospheric H_2O content could result from the lack of significant high-altitude methane on Uranus, which precludes shock chemistry reactions between the supplied H_2O and atmospheric CH_4 to form CO, making H_2O the preferred ablation product (Moses & Poppe 2017). Lara et al. (2019) further investigated oxygen chemistry on Uranus and also conclude that an ancient comet impact may have contributed to Uranus's CO, with the majority of stratospheric H_2O and CO_2 supplied by IDPs. However, lack of observational constraints on the water profile meant that results were inconclusive.

For Neptune, the observed stratospheric CO abundance is orders of magnitude greater than IDP model predictions (Poppe 2016; Moses & Poppe 2017). This suggests that a kilometer-scale comet impact is required to supply large quantities of stratospheric CO from shock chemistry, where water reacts with atmospheric CH_4 at high temperatures to give CO and H_2 (Lellouch et al. 2005; Hesman et al. 2007). An example of this is the SL9 impact, which injected large quantities of CO into Jupiter's stratosphere via reactions of cometary H_2O with atmospheric CH_4 (Lellouch 1996). A comet impact is also consistent with recent observation of CS in Neptune's stratosphere, another shock chemistry product, whose observed abundance of $(2.0–3.1) \times 10^{12}$ cm^{-2} implies a comet impact in the past few hundreds to thousands of years (Moreno et al. 2017). Therefore, unlike Uranus, multiple source processes must be invoked to explain Neptune's oxygen species observations. A further complication on Neptune is the higher abundance of CH_4 in its upper atmosphere, which may also favor CO as an IDP ablation product over H_2O, but this critically depends on the unknown IDP ablation temperature (Moses & Poppe 2017). To fit available H_2O, CO, and CO_2 observations on Neptune, oxygen species influxes had to be scaled to 2×10^5 cm^{-2} s^{-1} for H_2O, 2×10^8 cm^{-2} s^{-1} for CO, and 2×10^4 cm^{-2} s^{-1} for CO_2 (Moses & Poppe 2017). These H_2O and CO_2 fluxes are broadly compatible with Poppe (2016) and Moses & Poppe (2017) IDP flux model predictions, but CO flux is orders of magnitude too large and requires a comet impact with shock chemistry conversion to explain.

In summary, H_2O abundance has important implications for constraining external flux processes, especially if the vertical profile can be constrained. Here we use high spectral resolution and high signal-to-noise ratio observations by Herschel's Heterodyne Instrument for the Far-Infrared (HIFI) to improve constraints on Uranus's and Neptune's stratospheric water.

Table 1
Herschel-HIFI Observations

	Uranus	Neptune
ObsID	1342198318	1342196596
Date	15/6/2010	16/5/2010
Observational day	397	367
Start time (UTC)	01:46:51	12:36:47
Integration time (s)	8459	17963
LO frequency (GHz)†	550.44225	550.44450
LO frequency corr. (GHz)‡	550.38922	550.39067
Distance (au)	20.1873	30.0549
Relative velocity (km s^{-1})	+28.885	+29.321
Planet size (arcsec)	3.49	2.27
Sub-Herschel latitude (deg N)	13.2	−28.4
Sub-Herschel longitude (deg E)	114.3	177.7
North pole angle (deg)	254.3	334.5

Note. LO = local oscillator († telescope frame, ‡ planet frame); positive relative velocity indicates that the planet is moving toward Herschel; sub-Herschel latitude and longitude are planetocentric coordinates for disk center; north pole angle is the counterclockwise angle of the planet's north pole from celestial north.

2. Observations

Observations were taken in 2010 with the Herschel space telescope (Pilbratt et al. 2010) HIFI (de Graauw et al. 2010; Roelfsema et al. 2012), with preliminary analysis presented by Jarchow et al. (2010). The observations are part of the Herschel solar system Observations (HssO) key program (Hartogh et al. 2009) and are available from the Herschel Science Archive.[5] Observations targeted the 556.936 GHz H_2O line using HIFI's dual-beam-switch single-point observation mode (HIFI Observers' Manual 2011; Roelfsema et al. 2012). Uranus was observed for a total of 2.3 hr and Neptune for 5.0 hr. Both high-resolution spectrometer (HRS) and wide-band spectrometer (WBS) observations were taken simultaneously. The HRS has a 230 MHz bandwidth at 0.13 MHz spectral resolution (0.06 MHz sampling), and the WBS has a 4.1 GHz bandwidth at 1.1 MHz spectral resolution (0.5 MHz sampling). Observations are double-sideband (DSB) spectra, where frequency is measured relative to a local oscillator and the final spectrum is a combination of the folded lower-sideband (LSB) and upper-sideband (USB) spectra (de Graauw et al. 2010; Roelfsema et al. 2012). Calibration is via the standard v14.1.0 level 2.5 pipeline (Shipman et al. 2017), which outputs separate antenna temperatures T_A^* and associated error bars for vertical and horizontal polarizations for each of the HRS and WBS observations. Antenna temperatures are corrected for forward efficiency and beam efficiency by the pipeline (Shipman et al. 2017). Herschel's primary mirror has an effective diameter of 3.28 m, which at 557 GHz results in an Airy disk 41″ in diameter. This is large compared to the size of Uranus (3.″49) and Neptune (2.″27) and results in disk-averaged spectra. Further observation details are given in Table 1.

The observed water emission lines from both Uranus and Neptune are very narrow (∼10 MHz), so we primarily use the HRS observations to allow us to more fully resolve the line shape. The water line is in HIFI's USB, which for the local oscillator settings used here has a single-sideband gain of 0.516 for Uranus and 0.514 for Neptune. The intrinsic Doppler line width for water vapor at relevant temperatures (⩾125K) is always ⩾0.6 MHz (⩾2×10^{-5} cm^{-1}). Therefore, to increase the signal-to-noise ratio and computational efficiency of subsequent analysis, the HRS spectra were binned to a resolution of 0.6 MHz with a sample spacing of 0.3 MHz. The error on each binned data point was taken to be the standard error derived from the observation error bars of the points in each bin. WBS spectra were not binned and remained at 1.1 MHz resolution with a 0.5 MHz sample spacing.

HIFI observations are affected by well-documented ∼100 MHz continuum ripples (Roelfsema et al. 2012; Kester et al. 2014). These were fitted and removed prior to analysis using a procedure similar to Teanby et al. (2014). Briefly, this involved masking out the water line core and wings at 556.92–556.95 GHz, removing the mean antenna temperature, fitting a sine wave using least-squares linear inverse theory (Gubbins 2004), subtracting this sine wave, and then re-adding the mean antenna temperature to recover a corrected spectrum. Each HRS and WBS polarization was fitted and corrected separately.

To simplify subsequent analysis, the HRS and WBS spectra were converted from antenna temperature into line-to-continuum ratios. This has the added advantage of removing the influence of forward and beam efficiency assumptions in the pipeline from the spectra. First, the water line region from 556.92 to 556.95 GHz was masked and a linear continuum was fitted to the corrected spectra for each polarization. Higher-order polynomial continuum fits were not justified, as a linear continuum fitted the narrow spectral range to well within errors. Second, the full unmasked spectra were divided by the linear continuum fit to give a line-to-continuum ratio for each polarization. Finally, the corrected vertically and horizontally polarized spectra were combined into a single mean spectrum for each planet. The resulting final HRS and WBS DSB line-to-continuum spectra are shown in Figure 1. Both HRS and WBS data are consistent to within errors. Note that because these are DSB spectra, the HIFI pipeline normalizes the antenna temperature by the USB gain to preserve the emission-line height above the continuum:

$$T_A^*(f') = \frac{(1.0 - g_{\rm usb})T_A^*(f'_{\rm LO} - (f' - f'_{\rm LO})) + g_{\rm usb}T_A^*(f')}{g_{\rm usb}}, \quad (1)$$

where f' is sky frequency in the USB, $f'_{\rm LO}$ is the local oscillator frequency, $g_{\rm usb}$ is the USB gain (approximately 0.51), $(1.0 - g_{\rm usb})$ is the LSB gain, and $(f'_{\rm LO}–(f'–f'_{\rm LO}))$ is the LSB sky frequency. However, this normalization means that the continuum levels of HIFI's Level 2.5 antenna temperatures are approximately twice what they should be (Shipman et al. 2017). Therefore, after conversion of the spectra to line-to-continuum ratios, the peak height of the water line is roughly halved compared to a conventional line-to-continuum spectrum. This was not corrected for in the data, but instead is accounted for by explicitly including the sideband gains in the synthetic spectra forward modeling. Both Uranus and Neptune spectra have a flattened water emission peak, which is due to a combination of the disk-average nature of the spectra and Doppler shift from the planets' rotation. This effect is visible in both HRS and WBS spectra. Reconstructing this shape is discussed in detail in Section 3.3.

[5] http://archives.esac.esa.int/hsa/whsa/

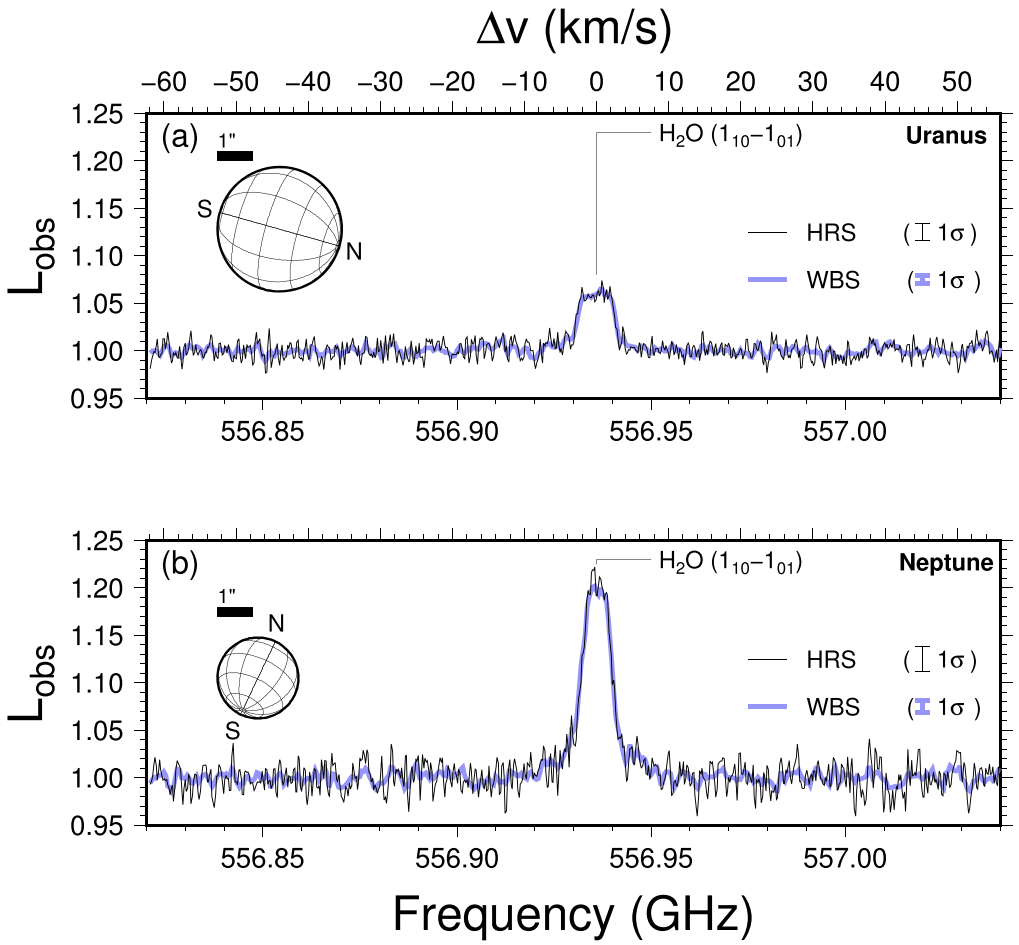

Figure 1. Herschel-HIFI water emission line disk-averaged HRS and WBS observations of (a) Uranus and (b) Neptune. DSB spectra have been converted to line-to-continuum ratio, with horizontal and vertical polarizations averaged together to give a single spectrum for each planet. HRS spectra have been binned at 0.6 MHz (0.3 MHz sample spacing) to increase signal-to-noise ratio. The error bar indicates mean 1σ uncertainty. HRS and WBS spectra are consistent to within errors. Insets show orientation of Uranus and Neptune during the observations with a $1''$ scale bar. Water emission lines are broadened by Doppler shift induced by planetary rotation. The data behind this figure are available.

(The data used to create this figure are available.)

3. Methods

3.1. Reference Atmospheres

To allow forward modeling of the Uranus and Neptune water emission spectra, we first construct reference atmospheres of temperature and composition on an evenly spaced 121-point logarithmic pressure grid from 100 bars to 0.1 nbar, with 10 levels per pressure decade. The main factors relevant for the spectral region considered here are temperature, He/H_2 ratio, and CH_4 abundance. For each planet, nominal, hot, and cold temperature profiles are constructed to account for uncertainties in the globally averaged temperature structure.

For Uranus the nominal temperature profile was compiled from 0.05 mbar to 0.1 nbar, combined Voyager UVS and stellar occultation "compromise profile" from Herbert et al. (1987); 2.3 bars to 0.25 mbar, Voyager RSS profile from Lindal et al. (1987) with discrete small-scale features in the 0.25–20 mbar region masked out because they exhibited high variability between ingress and egress profiles; and >2.3 bars, a downward extrapolation using the dry adiabatic lapse rate from Irwin (2009). Gaps in the temperature profile were linearly interpolated in log(pressure) space to avoid sharp bumps. Hot and cold profiles were generated using the uncertainties in Herbert et al. (1987) and Lindal et al. (1987). Furthermore, recent work suggests that Uranus's upper atmosphere temperature has cooled significantly since the Voyager era by as much as 250 K (Melin et al. 2011; Trafton et al. 2021). This change is incorporated into the cold profile, which results in a significantly different—and more Neptune-like—upper atmosphere temperature. An He/H_2 ratio of 0.1306 from Sromovsky et al. (2011) was assumed (F1 profile, their Table 1). The CH_4 profile was the combined fit to Herschel-PACS/Spitzer-IRS data from Lellouch et al. (2015).

For Neptune the nominal temperature profile was compiled from <1 nbar, Voyager UVS (Broadfoot et al. 1989); 0.3 μbar to 10 nbar, Voyager UVS (Yelle et al. 1993); 10 mbar to 1 μbar, AKARI mid-IR observations (Fletcher et al. 2010); 1.7 bar to 15 mbar, Voyager RSS (Lindal 1992); and >2 bar, using the dry adiabatic lapse rate profile from Luszcz-Cook & de Pater (2013). Again, small gaps in the profile were linearly interpolated in log(pressure) space. Hot and cold profiles were generated using the uncertainties given in (or estimated from) Broadfoot et al. (1989), Yelle et al. (1993), Fletcher et al. (2010), Lindal (1992), and Luszcz-Cook & de Pater (2013). He/H_2 was set to 0.15 based on Voyager measurements (Conrath et al. 1993). The CH_4 profile was taken from

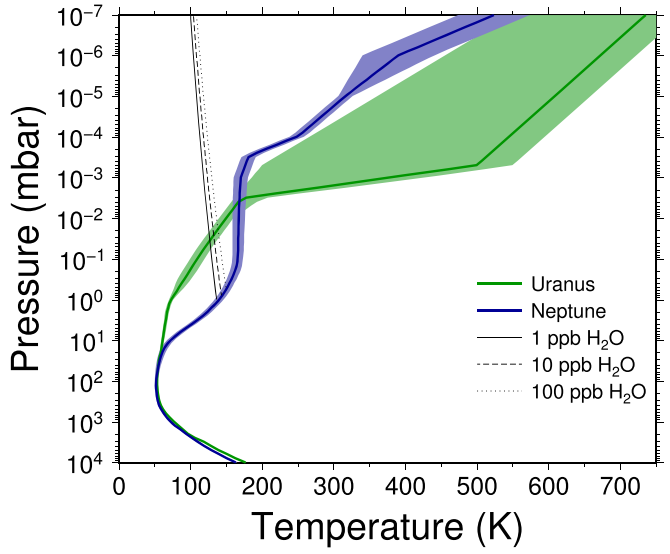

Figure 2. Uranus and Neptune atmospheric temperature profiles, including estimated uncertainties. The nominal profile for each planet is indicated by the solid line, whereas hot and cold profiles are indicated by extremes of the uncertainty envelopes. Note that for Uranus the low-temperature envelope includes upper atmosphere cooling (Melin et al. 2011; Trafton et al. 2021) in addition to measurement uncertainties. Black lines indicate temperature at 100% relative humidity for 1, 10, and 100 ppb water vapor. For colder atmospheric temperature, SVP is exceeded and condensation occurs. On Uranus the condensation level is ∼0.03 mbar, and on Neptune it is ∼1 mbar because of the warmer stratosphere. The data behind this figure are available.

(The data used to create this figure are available.)

Herschel-HIFI/PACS analysis (Lellouch et al. 2015), which had a deep abundance of 2% with SVP applied around the tropopause and a maximum stratospheric VMR set to 1.15×10^{-3}. Note that Neptune has around 10 times more stratospheric CH_4 than Uranus.

For both Uranus and Neptune, at each pressure level the H_2 and He abundance was adjusted such that VMRs of H_2, He, and CH_4 totaled unity. Altitudes were calculated assuming hydrostatic equilibrium and referenced to 0 km at the 1 bar pressure level.

The water profile on Uranus and Neptune is controlled by SVP, ablation, chemistry, and mixing processes. There is not enough information content in a disk-averaged spectrum to constrain all these processes, so we consider two types of parameterized profiles appropriate for externally sourced species: (1) simple step profiles with uniform VMR for pressures lower than a cutoff pressure, as is commonly used for other externally sourced species (Luszcz-Cook & de Pater 2013; Moreno et al. 2017); and (2) scaling of photochemical-model-predicted profiles from Moses & Poppe (2017) and Lara et al. (2019).

SVP is an important constraint on the water profiles. We ensured that our profiles were physically plausible by applying the SVP curve from Murphy & Koop (2005), which is based on low-temperature measurements at ⩾110 K. For reasonable water abundances in the 1–100 ppb range, water is predicted to condense at ∼0.03 mbar for Uranus (∼125 K) and ∼1 mbar for Neptune (∼140 K). Condensation curves are plotted along with the nominal, hot, and cold composite temperature profiles in Figure 2, which shows that condensation occurs at much lower pressure in Uranus's colder stratosphere than for Neptune's warmer stratosphere.

For Uranus, six uniform water profiles were tried: a profile with uniform VMR limited by SVP at high pressure; a step profile with a cutoff pressure of 0.01 mbar; and four profiles with cutoff pressures at 1.0, 0.6, 0.3, and 0.1 mbar, where saturation vapor was not applied in order to test whether supersaturation was required to fit the observations. We also tried rescaling model profiles from Moses & Poppe (2017) and Lara et al. (2019), with SVP applied after each scaling to ensure that the atmosphere did not become supersaturated. For the Moses & Poppe (2017) profile we used the model version where the external fluxes of H_2O, CO, and CO_2 were scaled to provide the best match to previous oxygen species observations (solid line profile in Moses & Poppe 2017, Figure 12). For Neptune, six uniform profiles were tried: five step profiles with cutoff pressures at 1, 0.6, 0.3, 0.1, and 0.01 mbar; and a uniform VMR profile limited by SVP at high pressure. We also tried rescaling the model profile from Moses & Poppe (2017), again with SVP applied after each scaling and using the version where the external flux of oxygen species has been scaled to give the best match to previous observations (solid line profile in Moses & Poppe 2017, Figure 13). Note that we prefer to use the Moses & Poppe (2017) model where oxygen species fluxes have been rescaled to fit previous water measurements, as these models have an atmospheric composition closest to the actual planetary compositions, so the photochemical schemes will be more appropriate.

3.2. Spectroscopic Parameters

Spectroscopic data for the water lines were from the GEISA 2020 line database (Delahaye et al. 2021). However, the air-broadened Lorentz line widths and associated temperature dependences from GEISA were replaced with a fit to the more appropriate He and H_2 broadened widths for the 557 GHz water line measured by Dick et al. (2009). From these measurements we calculated a combined fit to the Lorentz width γ and temperature dependence $n_{\rm tdep}$ assuming an He/H_2 ratio of 0.15 for the temperature range 100–300 K, appropriate for Uranus's and Neptune's water-line-forming region. This gave a Lorentz width of $\gamma = \gamma_0 (p/p_0)(T_0/T)^{n_{\rm tdep}}$ with fitted values $\gamma_0 = 0.081\ {\rm cm}^{-1}$ and $n_{\rm tdep} = 0.61$, reference pressure $p_0 =$ 1 atm, and reference temperature $T_0 = 296$ K. Note that Neptune's He/H_2 ratio was assumed during this calculation, as pressure broadening is more important on Neptune because water vapor potentially exists at higher pressures than in Uranus's colder atmosphere, where Doppler line widths dominate. For example, the Lorentz width on Neptune for conditions around the saturation level (∼1 mbar, ∼140 K) is ∼4 MHz, and for Uranus (∼0.03 mbar, ∼125 K) it is ∼0.1 MHz. For comparison, the Doppler line width at ∼125 K is ∼0.6 MHz for water vapor. Continuum effects from collision-induced absorption for pairwise combinations of H_2, He, and CH_4 were included using the following parameterizations: H_2–H_2 (Fletcher et al. 2018), H_2–CH_4 (Borysow & Frommhold 1986), CH_4–CH_4 (Borysow & Frommhold 1987), and H_2–He (Borysow et al. 1988).

3.3. Disk-average Spectra Generation

Synthetic spectra for the Uranus and Neptune reference atmospheres were generated using the NEMESIS radiative transfer code (Irwin et al. 2008) and the line-by-line method (Goody & Yung 1989; Irwin 2009). During generation of the

synthetic spectra, careful consideration was given to the disk-average nature of the observations. The observed H_2O emission line is significantly broader than the intrinsic Lorentz and Doppler line widths because of the Doppler shift induced by the planets' rotation. This can be seen in Figure 1, where line widths for both planets are ~10 MHz. Therefore, in these observations rotation period is the controlling factor on observed line widths. Estimates of the internal rotation periods have been determined by fitting the periodicities of radio emission and magnetic fields in Voyager flyby observations, which are 17.24 hr for Uranus (Desch et al. 1986; Warwick et al. 1986) and 16.11 hr for Neptune (Warwick et al. 1989). However, the Voyager rotation periods do not account for atmospheric winds, which are significant on these planets. Helled et al. (2010) determined alternative rotation periods by minimizing the wind velocities and obtained 16.58 hr for Uranus and 17.46 hr for Neptune. Therefore, the rotation periods determined by Helled et al. (2010) are most appropriate for determining the observed line shape and are what we use in our analysis. As a simple test of the effects of rotation on line shape, the frequency shift induced by rotation can be estimated from the rotation period, equatorial radius, and observation frequency. For the 557 GHz water line the rotational Doppler shift for Uranus (equatorial radius 25,559 km) is ± 2.69 km s^{-1} (± 5.00 MHz), and for Neptune (equatorial radius 24,766 km) it is ± 2.48 km s^{-1} (± 4.61 MHz), when using the Helled et al. (2010) rotation periods. These Doppler shift values approximately match the observed ~10 MHz line widths, which confirms that rotationally induced Doppler shift is an important factor in the observed line shape. This effect is incorporated into the synthetic spectra generation as follows.

Forward modeling shows that on Uranus and Neptune limb brightening can lead to large radiances just off the planet limb and rapid changes in emitted radiance with emission angle, especially for the water emission line (Figure 3). Therefore, to accurately model rotationally induced Doppler shift in the observed spectra, it is important to consider radiance generated both on and off the planet's limb when forming a disk average. To do this, we defined a synthetic 1000×1000 pixel image grid covering a region 1.25 times the diameter of each planet to include both the on-disk and limb emission. The geometrical properties of each pixel (latitude, longitude, emission angle, tangent altitude) were calculated following the method of Teanby (2009). We assumed an oblate spheroid for each planet with equatorial and polar radii from JPL Horizons (Giorgini et al. 1996) and the reference surface for these radii defined at 1 bar. The bottom of the atmosphere in our model was set to 100 bars, with a corresponding altitude calculated from hydrostatic equilibrium. Any pixels with a tangent point below the bottom of the atmosphere were calculated as nadir spectra, with an emission angle defined at the bottom of the atmosphere. Any pixels with a tangent point above the bottom of the atmosphere were calculated as limb spectra. This ensured a smooth radiance transition from on-disk to off-disk pixels because 100 bars is well below the level of any emission in this spectral range. For simplicity, line-of-sight velocity for each pixel was calculated by assuming uniform solid-body rotation extending throughout the atmosphere. Spectra for each pixel were shifted using the velocity at the tangent point for off-disk pixels or the 1 bar level for on-disk pixels. This ignores the effect of the alternating east–west zonal jets on each planet. However, the line-of-sight velocity due to planetary rotation (2–3 km s^{-1}) dominates over eastward and westward zonal jets, which have wind speeds of up to a few hundred meters per second at most (Uranus: Karkoschka 2015; Sromovsky et al. 2015; Neptune: Sromovsky et al. 1993).

Once the geometry of each pixel in the grid was calculated, a synthetic spectrum was generated using NEMESIS for each pixel and a Doppler shift corresponding to the line-of-sight velocity applied. To avoid having to run a synthetic spectrum at each of the 10^6 pixel locations, we instead calculated ~300 synthetic spectra on a grid of impact parameter, i.e., offset of the line of sight from the planet center, covering the planet center to off-limb points at the top of the atmosphere, where the radiance emission has become negligible. For Uranus 314 grid points were used from the planet center to 1400 km above the 1 bar pressure level, and for Neptune 313 grid points were used from the planet center to 1400 km above the 1 bar pressure level, which more than covered the region of significant radiance emission (Figure 3). The grid spacing in each case was variable, being coarsely spaced (500 km) in the disk center, where radiance changes are small (for impact parameters <21,000 km, or emission angles <58°), and reduced progressively to 5–100 km around the limb to give an accurate reproduction of radiance dependence on impact parameter (as indicated in Figure 3). The radiance at each of the 10^6 pixel locations was then interpolated in terms of an equivalent impact parameter derived from the emission angle (nadir pixels) or tangent altitude (limb pixels). Interpolation of the nadir spectra in terms of emission angle allowed us to account for the oblate shape of each planet correctly. The Doppler shift for the pixel line-of-sight velocity was then applied. This method increased the computational efficiency by a factor of ~3000 and made the analysis practical. Once the synthetic image was calculated, the radiance was multiplied by the normalized Airy disk response of Herschel's 3.28 m main mirror, and the contributions from all pixels summed to give the disk-averaged radiance spectrum. As a check, we converted these synthetic spectra into Janskys using the method of Teanby et al. (2013) and compared them to the observed antenna temperatures, also converted into Janskys using the conversion factors in HIFI Observers' Manual (2011). The continuum level was well within the expected ~10% absolute calibration accuracy of HIFI stated by Roelfsema et al. (2012).

For direct comparison with the HIFI observations, each synthetic disk-averaged spectrum was converted into a DSB spectrum. First, the disk-averaged spectrum $y(f)$ was Doppler shifted by the relative velocity between Herschel and Uranus or Neptune to convert it into what would be seen by the telescope $y(f')$, where f is frequency in the planet frame and f' is Doppler-shifted frequency seen by the telescope (sky frequency). Second, a synthetic DSB spectrum $y_{\rm dsb}(f')$ was generated by folding the spectrum about HIFI's local oscillator frequency $f'_{\rm LO}$ (also in the telescope frame), with the resulting synthetic spectrum in the telescope frame given by

$$y_{\rm dsb}(f') = (1.0 - g_{\rm usb})y(f'_{\rm LO} - (f' - f'_{\rm LO})) + g_{\rm usb}y(f'), \quad (2)$$

where $g_{\rm usb}$ is the single-sideband gain for the USB, 0.516 for Uranus and 0.514 for Neptune (Roelfsema et al. 2012). It is important to perform the spectral folding in the telescope frame to correctly reproduce the HIFI spectrum because the continuum has a slight gradient. Third, the spectrum was Doppler shifted back into the planet frame to give $y_{\rm dsb}(f)$

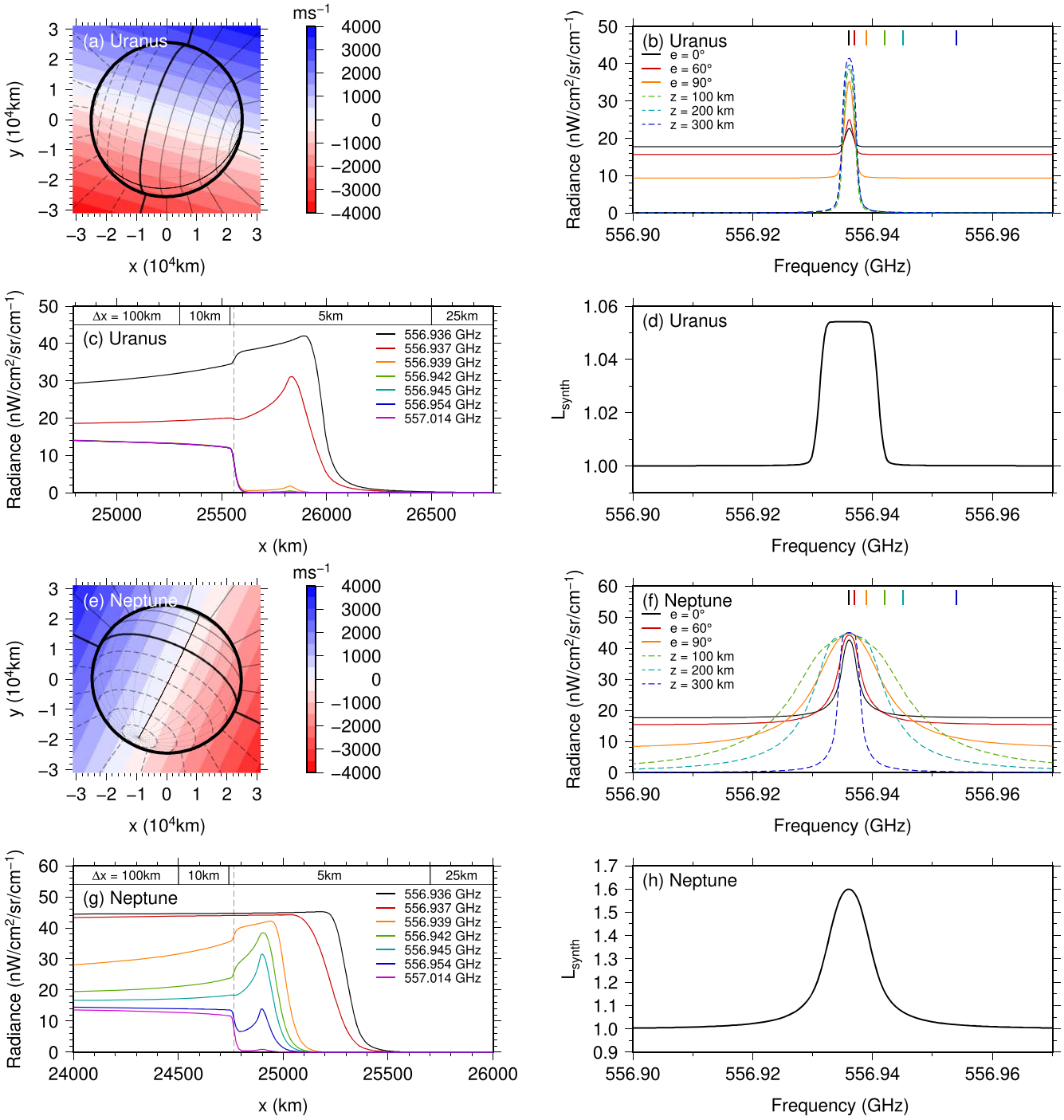

Figure 3. Generation of disk-averaged synthetic spectra for (a–d) Uranus and (e–h) Neptune. (a, e) Synthetic 1000 × 1000 pixel image covering the on- and off-disk regions, with lines of latitude (black lines spaced by 15°) and line-of-sight velocity (colors) assuming Helled et al. (2010) rotation rates and solid-body rotation. (b, f) Synthetic single-pixel radiance spectra for on-disk points with emission angles $e = 0°$, 60°, and 90° and limb spectra with tangent altitudes of 100, 200, and 300 km above the 1 bar pressure level. There is significant radiance emitted off the planet limbs, especially for the 556.936 GHz water emission line. (c, g) Radiance as a function of impact parameter x (offset from planet center) for water emission line center at 556.936 GHz and wing regions indicated in panels (b) and (f) with colored vertical bars. The dashed vertical line indicates a radius of 1 bar pressure level. At around ∼1000 km off the planet limb the emitted radiance becomes negligible. Grid spacing of synthetic spectra is indicated by Δx. (d, h) Composite line-to-continuum ratio spectra from combining contributions from 10^6 image pixels with Airy disk weighting.

because the Level 2.5 HIFI data are also corrected into the planet frame by the pipeline processing. Finally, the synthetic spectrum was converted into a line-to-continuum spectrum $L_{\rm synth}(f)$ using the same method as in Section 2. The resulting disk-averaged DSB line-to-continuum ratio synthetic spectra are directly comparable to the observations.

3.4. Fitting Procedure

To fit the observations, we used a forward modeling χ^2 minimization procedure similar to Teanby et al. (2019). This involved defining the water profile either as a uniform step-type profile or as a profile from an atmospheric model and then grid searching to find the abundance or scale factor s that minimized

the χ^2 misfit value between observed and synthetic spectra:

$$\chi^2(s) = \sum_{i=1}^{N} \left[\frac{L_{\rm obs}(f_i) - L_{\rm synth}(f_i, s)}{\sigma(f_i)} \right]^2, \quad (3)$$

where s is the abundance or scale factor for the H_2O profile, $L_{\rm obs}(f_i)$ is the observed line-to-continuum DSB spectrum, $L_{\rm synth}(f_i, s)$ is the disk-averaged line-to-continuum DSB synthetic spectrum, and $\sigma(f_i)$ are the line-to-continuum observational errors, for N frequencies f_i ($i = 1 \ldots N$). For a given assumed water profile shape, the best-fitting profile abundance or scale factor s_0 has the minimum misfit χ_0^2. If the synthetic spectrum fits the observations to within error, then $\chi_0^2/N \sim 1$. The 1σ uncertainty on s corresponds to $(\Delta f_{\rm obs}/\Delta f_{\rm res})(\chi^2(s) - \chi_0^2) = +1$ (Press et al. 1992), where $\Delta f_{\rm obs}$ is the HIFI sample spacing after binning (0.3 MHz) and $\Delta f_{\rm res}$ is the spectral resolution after binning (0.6 MHz). The factor $\Delta f_{\rm obs}/\Delta f_{\rm res}$ is 0.5 in this case and corrects for data oversampling, as there are twice as many spectral points as there are independent measurements. The significance of any differences in spectral fits between using different water profiles can be determined from changes in $(\Delta f_{\rm obs}/\Delta f_{\rm res})\chi_0^2$; differences of <16 are indistinguishable at the 4σ level, whereas differences $\geqslant 16$ indicate a profile that results in a significantly worse fit that can be rejected (Press et al. 1992).

4. Results

Figure 4 shows best-fitting synthetic spectra for different water vapor profile types on Uranus and Neptune. Scale factors for photochemical model profiles (Moses & Poppe 2017; Lara et al. 2019) and VMRs for step profiles are given in Table 2, along with associated integrated column abundances and χ_0^2/N values. Profiles with χ_0^2/N close to unity indicate that the spectral fit is consistent with observational errors, although these are effectively averaged misfit values over a large spectral range covering mostly continuum, so they are not particularly sensitive to water line fit quality. Instead, we use differences in $(\Delta f_{\rm obs}/\Delta f_{\rm res})\chi_0^2$ compared to the best-fitting profile to determine whether fits are acceptable. Values for the nominal, cold, and hot temperature profiles are given separately in Table 2. Table 3 gives combined abundances for each profile type along with uncertainties that incorporate observational errors in the HIFI spectra and temperature uncertainties from the cold and hot end-member temperature profiles.

For Uranus, an acceptable fit to observations is obtained by scaling both photochemical models and step-type profiles that have cutoff pressures of 0.6 mbar or less. Only the 1 mbar step profile could be rejected, as the resulting spectral line had too much pressure broadening to be consistent with observations. Uranus's condensation level is ~0.03 mbar, so the observations themselves do not rule out supersaturation, but we regard this as highly unlikely. Instead, we prefer to use saturation level as an additional constraint on Uranus's water profile, which limits water vapor to pressures less than ~0.03 mbar. At these low pressures the water emission line is intrinsically very narrow. Therefore, line shape is dominated by planetary-rotation-induced Doppler shift, and the exact form of the vertical water profile has little effect. The dominance of planetary rotation in determining line shape results in the characteristic flat-topped emission line in the disk-averaged spectrum. For a uniform profile limited by SVP the column abundance is $0.54^{+0.05}_{-0.06} \times 10^{14}$ cm^{-2}. This is equivalent to a VMR of $5.3^{+3.5}_{-2.5}$ ppb, although, as seen in Tables 2 and 3, this value is very sensitive to profile step pressure, so column abundance is a more robust quantity. Both Moses & Poppe (2017) and Lara et al. (2019) photochemical profiles also provide excellent fits to the observations but require scaling by factors of $0.73^{+0.34}_{-0.04}$ and $1.25^{+0.79}_{-0.41}$, respectively, to fit the data. The full range of column water abundance for all profiles consistent with the observations is $0.54^{+0.26}_{-0.06} \times 10^{14}$ cm^{-2}, which includes the uncertainty on Uranus's temperature profile.

For Neptune, which has a warmer stratosphere than Uranus, a wider scope of vertical profiles is possible. Water vapor can exist at higher pressures in Neptune's stratosphere, so Lorentz pressure broadening has a significant effect on emission-line shape, which results in a more rounded overall line shape in the disk-averaged spectrum. For step-type profiles the best fit is obtained with a step pressure of 0.3 or 0.6 mbar, giving a column abundance of $(1.9 \pm 0.2) \times 10^{14}$ cm^{-2}, equivalent to 2.2 ± 0.3 ppb for a 0.3 mbar step or 1.1 ± 0.1 ppb for a 0.6 mbar step. These are lower pressures than the ~1 mbar condensation level predicted by SVP and imply that observations contain information about water's vertical profile. Indeed, step pressures $\geqslant$1.0 mbar or $\leqslant$0.1 mbar provide a significantly worse fit to observations and can be rejected at the 4σ level (Figure 4 and Table 2). An excellent fit is also obtained by scaling the Moses & Poppe (2017) photochemical profile by $0.63^{+0.07}_{-0.08}$, resulting in a column abundance of $(1.9 \pm 0.2) \times 10^{14}$ cm^{-2}. The full range of column water abundance for the Moses & Poppe (2017) photochemical profile and the 0.3 and 0.6 mbar uniform step profiles is $1.9^{+0.2}_{-0.3} \times 10^{14}$ cm^{-2} including the uncertainty on Neptune's temperature profile.

5. Discussion

For Uranus, our stratospheric water column abundance of $0.54^{+0.26}_{-0.06} \times 10^{14}$ cm^{-2} is consistent with the value of $(0.5–1.2) \times 10^{14}$ cm^{-2} found by ISO-SWS (Feuchtgruber et al. 1997). For Neptune, our value of $1.9^{+0.2}_{-0.3} \times 10^{14}$ cm^{-2} is consistent with $(2–6) \times 10^{14}$ cm^{-2} from ISO-SWS (Feuchtgruber et al. 1997) and also with a more recent determination of $(2.1 \pm 0.5) \times 10^{14}$ cm^{-2} using Herschel-PACS (Lellouch et al. 2010). We note that both our estimates and those of Lellouch et al. (2010) are at the lower end of the Feuchtgruber et al. (1997) uncertainty range. Observational results presented here are significantly more precise than previous determinations owing to the increased signal-to-noise ratio and spectral resolution of Herschel-HIFI. Our observations show that column abundance of water is about four times greater on Neptune than on Uranus.

Our results only provide modest constraints on water profile shapes. For Uranus, scaled photochemical model profiles from Moses & Poppe (2017) or Lara et al. (2019) fit the spectrum very well, as do step-type profiles so long as water vapor is limited to pressures $\leqslant$0.6 mbar. However, Uranus's cold stratosphere causes SVP to be exceeded at pressures higher than ~0.03 mbar, so significant water vapor at higher pressures would require unrealistically extreme supersaturation. For example, 0.5 ppb water vapor at 0.3 mbar (~90 K) would have an SVP of $\sim 10^{-17}$ Pa (Murphy & Koop 2005), which would be supersaturated by a factor of $\sim 10^9$. Therefore, we assume that Uranus's stratospheric water is limited to pressures $\leqslant$0.03 mbar. This implies that Uranus's spectral line shape is

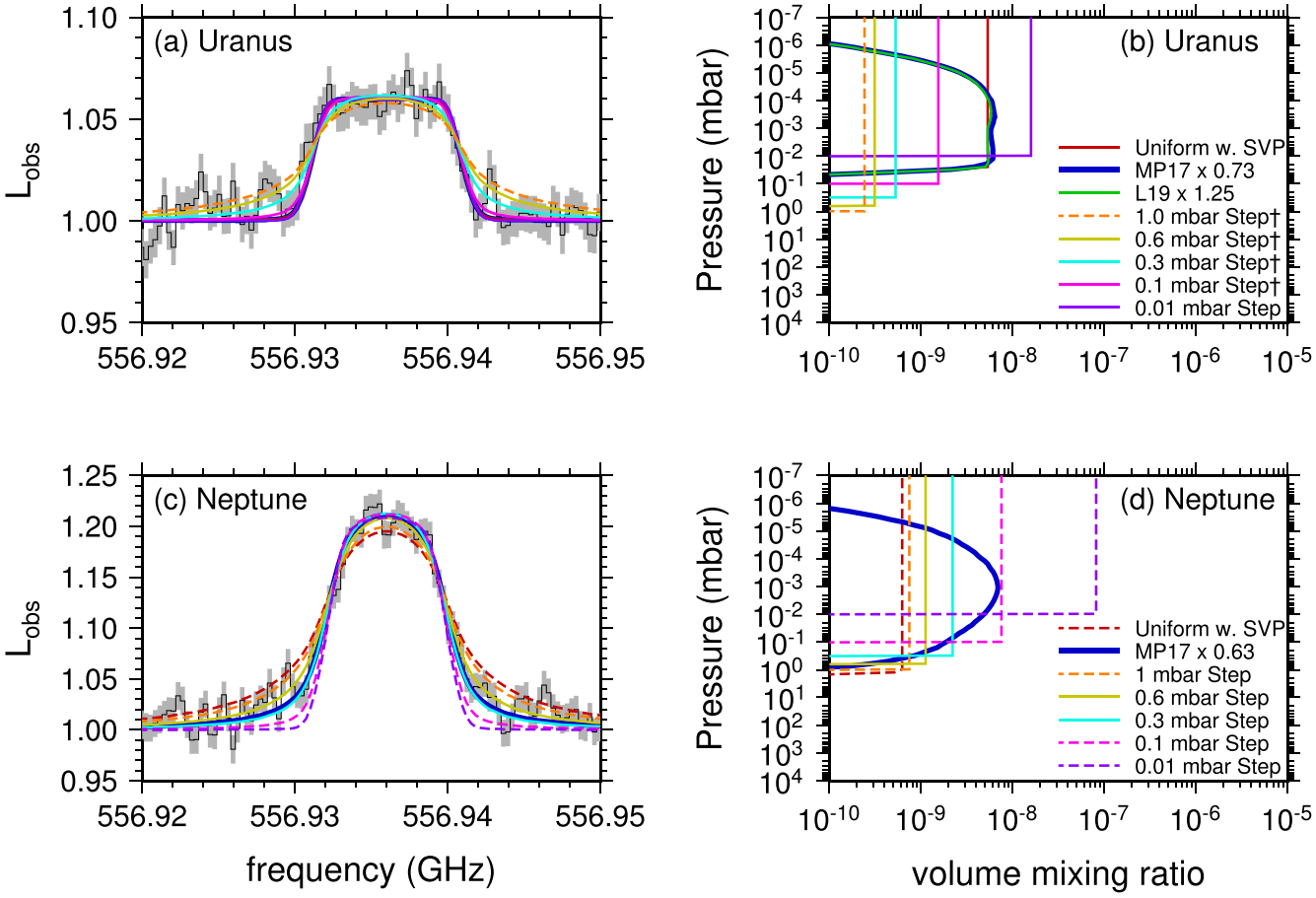

Figure 4. Fitted water profiles to observed HIFI HRS line-to-continuum spectra for (a, b) Uranus and (c, d) Neptune using the nominal temperature profile. (a, c) The black line shows observed spectra with 1σ error envelope in gray. Colored lines in panels (a) and (c) correspond to synthetic spectra generated with best-fitting water profiles shown in panels (b) and (d). MP17 = Moses & Poppe (2017) profiles; L19 = Lara et al. (2019) profiles. Profiles shown with solid lines provide excellent fits to observed spectra that are indistinguishable from the best-fitting profile at 4σ significance, whereas dashed lines produce significantly worse fits and can be rejected with 4σ significance. For Uranus, all profiles fit observations well except the 1 mbar step. For Neptune, the 0.3 and 0.6 mbar step and scaled Moses & Poppe (2017) profiles produce significantly better fits (Table 2).

dominated by planetary rotation and there is limited information on the water profile. For Neptune, the warmer stratosphere allows a wider range of possible profiles, as saturation does not occur until pressures above ~1 mbar. Scaling the photochemical model profile from Moses & Poppe (2017) provides an excellent fit to the Neptune spectrum, as do step-type profiles with cutoffs of ~0.3–0.6 mbar. Therefore, water vapor is present much deeper in Neptune's stratosphere than in Uranus's.

Our observed water column abundances can also be compared to those in photochemical models to infer external water flux. Moses & Poppe (2017) calculate water profiles for Uranus and Neptune using a source term based on an ablation and photochemical model, combined with a source flux of IDP grains modified from the dynamical model predictions of Poppe (2016). The ablation model component of Moses & Poppe (2017) predicts oxygen atom fluxes of $8.9^{+19}_{-6.1} \times 10^4\,\mathrm{cm^{-2}\,s^{-1}}$ for Uranus and $7.5^{+16}_{-5.1} \times 10^5\,\mathrm{cm^{-2}\,s^{-1}}$ for Neptune. These are slightly different from predictions in Poppe (2016) because Moses & Poppe (2017) extrapolate IDP distribution to larger grain sizes and only consider the component released into the atmosphere by ablation. External oxygen is expected to comprise a mixture of water, carbon monoxide, and carbon dioxide components, but exact composition is unknown, so typically fluxes of each species must be scaled in photochemical models to fit observations. Moses & Poppe (2017) found that the photochemical model required external water fluxes of $1.2 \times 10^5\,\mathrm{cm^{-2}\,s^{-1}}$ for Uranus and $2 \times 10^5\,\mathrm{cm^{-2}\,s^{-1}}$ for Neptune to fit previous observations (solid line profiles in Moses & Poppe 2017, Figures 12 and 13). Integrating these model profiles gives total column water abundances of $0.78 \times 10^{14}\,\mathrm{cm^{-2}}$ for Uranus and $3.0 \times 10^{14}\,\mathrm{cm^{-2}}$ for Neptune. Our observed overall column abundances from Herschel/HIFI are $0.54^{+0.26}_{-0.06} \times 10^{14}\,\mathrm{cm^{-2}}$ for Uranus and $1.9^{+0.2}_{-0.3} \times 10^{14}\,\mathrm{cm^{-2}}$ for Neptune (Table 3). Using a simple scaling, our observations imply external H_2O fluxes of $8.3^{+4.0}_{-0.9} \times 10^4\,\mathrm{cm^{-2}\,s^{-1}}$ for Uranus and $12.7^{+1.3}_{-2.0} \times 10^4\,\mathrm{cm^{-2}\,s^{-1}}$ for Neptune. This assumes that photochemical processing of H_2O occurs according to the scheme in Moses & Poppe (2017).

For Uranus, our inferred external water flux of $8.3^{+4.0}_{-0.9} \times 10^4\,\mathrm{cm^{-2}\,s^{-1}}$ is very close to the predicted total oxygen atom flux of $8.9^{+19}_{-6.1} \times 10^4\,\mathrm{cm^{-2}\,s^{-1}}$ from Moses & Poppe (2017). Moses & Poppe (2017) point out that sluggish circulation in Uranus's stratosphere and mesosphere, combined with cold temperatures, means that methane sourced from the deep atmosphere decreases significantly in abundance for pressures less than ~0.1 mbar. As ice ablation peaks higher up at 10^{-2}–10^{-6} mbar on Uranus, there is expected to be limited interaction between atmospheric hydrocarbons and water

Table 2
Best-fitting Water Profiles for Nominal, Cold, and Hot Temperature Profiles

Planet	Rot. Period[a] (hr)	Profile	VMR (ppb)	Scale Factor	Column (10^{14} molecules cm^{-2})	χ_0^2/N	$\frac{\Delta f_{obs}}{\Delta f_{res}}\chi_0^2$	$\Delta\sigma^2$
Nominal	⋯		⋯	⋯	⋯	⋯	⋯	⋯
Uranus	16.58	Uniform w. SVP	5.31 ± 0.30	⋯	0.54 ± 0.03	0.910	344.1	7.5[b]
Uranus	16.58	1.0 mbar step[a]	0.24 ± 0.01	⋯	0.85 ± 0.04	0.948	358.2	21.6[c]
Uranus	16.58	0.6 mbar step[a]	0.31 ± 0.02	⋯	0.69 ± 0.03	0.911	344.4	7.8[b]
Uranus	16.58	0.3 mbar step[a]	0.53 ± 0.03	⋯	0.58 ± 0.03	0.891	336.6	0.0[b]
Uranus	16.58	0.1 mbar step[a]	1.54 ± 0.08	⋯	0.54 ± 0.03	0.899	339.8	3.2[b]
Uranus	16.58	0.01 mbar step	15.85 ± 0.75	⋯	0.57 ± 0.03	0.912	344.6	8.0[b]
Uranus	16.58	Moses & Poppe (2017)	⋯	0.73 ± 0.04	0.54 ± 0.03	0.910	344.1	7.5[b]
Uranus	16.58	Lara et al. (2019)	⋯	1.25 ± 0.07	0.54 ± 0.03	0.910	344.1	7.5[b]
Neptune	17.46	Uniform w. SVP	0.63 ± 0.02	⋯	2.07 ± 0.06	1.196	454.6	57.6[c]
Neptune	17.46	1.0 mbar step	0.75 ± 0.02	⋯	1.97 ± 0.05	1.112	422.7	25.7[c]
Neptune	17.46	0.6 mbar step	1.13 ± 0.03	⋯	1.89 ± 0.05	1.045	397.0	0.0[b]
Neptune	17.46	0.3 mbar step	2.22 ± 0.06	⋯	1.87 ± 0.05	1.081	410.8	13.8[b]
Neptune	17.46	0.1 mbar step	7.55 ± 0.25	⋯	2.02 ± 0.07	1.218	462.9	65.9[c]
Neptune	17.46	0.01 mbar step	81.90 ± 3.26	⋯	2.22 ± 0.09	1.350	513.1	116.1[c]
Neptune	17.46	Moses & Poppe (2017)	⋯	0.63 ± 0.02	1.88 ± 0.05	1.065	404.7	7.7[b]
Cold	⋯		⋯	⋯	⋯	⋯	⋯	⋯
Uranus	16.58	Uniform w. SVP	8.31 ± 0.45	⋯	0.50 ± 0.03	0.913	345.1	8.4[b]
Uranus	16.58	1.0 mbar step[a]	0.27 ± 0.01	⋯	0.95 ± 0.05	0.955	360.9	24.2[c]
Uranus	16.58	0.6 mbar step[a]	0.35 ± 0.02	⋯	0.76 ± 0.04	0.915	345.7	9.0[b]
Uranus	16.58	0.3 mbar step[a]	0.56 ± 0.03	⋯	0.62 ± 0.03	0.891	336.7	0.0[b]
Uranus	16.58	0.1 mbar step[a]	1.53 ± 0.08	⋯	0.54 ± 0.03	0.899	339.7	3.0[b]
Uranus	16.58	0.01 mbar step	14.08 ± 0.69	⋯	0.50 ± 0.02	0.913	345.3	8.6[b]
Uranus	16.58	Moses & Poppe (2017)	⋯	1.02 ± 0.06	0.50 ± 0.03	0.913	345.1	8.4[b]
Uranus	16.58	Lara et al. (2019)	⋯	1.93 ± 0.10	0.50 ± 0.03	0.913	345.1	8.4[b]
Neptune	17.46	Uniform w. SVP	0.72 ± 0.02	⋯	1.80 ± 0.05	1.105	420.0	22.8[c]
Neptune	17.46	1.0 mbar step	0.74 ± 0.02	⋯	1.79 ± 0.05	1.096	416.6	19.4[c]
Neptune	17.46	0.6 mbar step	1.02 ± 0.03	⋯	1.71 ± 0.04	1.045	397.2	0.0[b]
Neptune	17.46	0.3 mbar step	2.02 ± 0.05	⋯	1.70 ± 0.05	1.079	410.0	12.8[b]
Neptune	17.46	0.1 mbar step	6.88 ± 0.23	⋯	1.84 ± 0.06	1.218	462.8	65.6[c]
Neptune	17.46	0.01 mbar step	76.00 ± 3.13	⋯	2.05 ± 0.08	1.356	515.4	118.2[c]
Neptune	17.46	Moses & Poppe (2017)	⋯	0.57 ± 0.02	1.71 ± 0.05	1.063	404.0	6.8[b]
Hot	⋯		⋯	⋯	⋯	⋯	⋯	⋯
Uranus	16.58	Uniform w. SVP	3.01 ± 0.19	⋯	0.56 ± 0.04	0.906	342.3	5.8[b]
Uranus	16.58	1.0 mbar step[a]	0.23 ± 0.01	⋯	0.80 ± 0.04	0.943	356.3	19.8[c]
Uranus	16.58	0.6 mbar step[a]	0.30 ± 0.01	⋯	0.66 ± 0.03	0.908	343.2	6.7[b]
Uranus	16.58	0.3 mbar step[a]	0.52 ± 0.02	⋯	0.57 ± 0.03	0.890	336.5	0.0[b]
Uranus	16.58	0.1 mbar step[a]	1.56 ± 0.08	⋯	0.55 ± 0.03	0.899	339.9	3.4[b]
Uranus	16.58	0.01 mbar step	16.86 ± 0.78	⋯	0.60 ± 0.03	0.910	344.1	7.6[b]
Uranus	16.58	Moses & Poppe (2017)	⋯	0.73 ± 0.04	0.56 ± 0.03	0.909	343.6	7.1[b]
Uranus	16.58	Lara et al. (2019)	⋯	0.89 ± 0.04	0.56 ± 0.03	0.907	342.7	6.2[b]
Neptune	17.46	Uniform w. SVP	0.57 ± 0.02	⋯	2.36 ± 0.08	1.312	498.7	101.9[c]
Neptune	17.46	1.0 mbar step	0.81 ± 0.02	⋯	2.16 ± 0.05	1.107	420.8	24.0[c]
Neptune	17.46	0.6 mbar step	1.23 ± 0.03	⋯	2.07 ± 0.05	1.044	396.8	0.0[b]
Neptune	17.46	0.3 mbar step	2.44 ± 0.07	⋯	2.05 ± 0.06	1.083	411.4	14.6[b]
Neptune	17.46	0.1 mbar step	8.24 ± 0.26	⋯	2.21 ± 0.07	1.218	463.0	66.2[c]
Neptune	17.46	0.01 mbar step	88.00 ± 3.42	⋯	2.38 ± 0.09	1.344	510.9	114.1[c]
Neptune	17.46	Moses & Poppe (2017)	⋯	0.68 ± 0.02	2.06 ± 0.05	1.067	405.3	8.5[b]

Notes.
[a] An SVP limit was not applied to these profiles. $\Delta\sigma^2$ is change in $(\Delta f_{obs}/\Delta f_{res})\chi_0^2$ compared to the profile with the lowest χ_0^2 misfit.
[b] Best-fitting profiles that are indistinguishable at 4σ significance from the model with the lowest χ_0^2 (i.e., $\Delta\sigma^2 < 16$); any of these models can be considered an acceptable fit to observations.
[c] Fits that can be rejected at 4σ significance, as they produce a significantly worse fit than the best-fitting model.

vapor, so measured water abundance is likely to be representative of the external source. However, if all ablated material is released as H_2O, then insufficient CO and CO_2 are supplied to explain their observed stratospheric abundances (Cavalié et al. 2014; Orton et al. 2014). Therefore, to reconcile observed abundances of all three of Uranus's main oxygen species (H_2O, CO, and CO_2), there are two options: (1) All oxygen species could be supplied solely by ablation of IDP grains. In this scenario grains would need to be $\sim 1/3$ H_2O, $\sim 2/3$ CO, and $\sim 1\%$ CO_2 to match observations, as suggested

Table 3
Best-fitting Water Profiles and Uncertainties

Planet	Profile	VMR (ppb)	Range (ppb)	Scale Factor	Range	Column (10^{14} molecules cm^{-2})	Range (10^{14} molecules cm^{-2})
Uranus	Uniform w. SVP	5.31	2.82–8.76	⋯	⋯	0.54	0.48–0.59[a]
Uranus	1.0 mbar step[c]	0.24	0.22–0.29	⋯	⋯	0.85	0.76–1.00[b]
Uranus	0.6 mbar step[c]	0.31	0.28–0.36	⋯	⋯	0.69	0.63–0.80[a]
Uranus	0.3 mbar step[c]	0.53	0.49–0.59	⋯	⋯	0.58	0.54–0.65[a]
Uranus	0.1 mbar step[c]	1.54	1.45–1.64	⋯	⋯	0.54	0.51–0.58[a]
Uranus	0.01 mbar step	15.85	13.39–17.64	⋯	⋯	0.57	0.48–0.63[a]
Uranus	Moses & Poppe (2017)	⋯	⋯	0.73	0.69–1.07	0.54	0.48–0.59[a]
Uranus	Lara et al. (2019)	⋯	⋯	1.25	0.84–2.04	0.54	0.48–0.58[a]
Uranus	**Combined H_2O column**	⋯	⋯	⋯	⋯	$\mathbf{0.54}^{+0.26}_{-0.06}$	
Neptune	Uniform w. SVP	0.63	0.55–0.74	⋯	⋯	2.07	1.74–2.44[b]
Neptune	1.0 mbar step	0.75	0.72–0.83	⋯	⋯	1.97	1.74–2.21[b]
Neptune	0.6 mbar step	1.13	1.00–1.26	⋯	⋯	1.89	1.67–2.12[a]
Neptune	0.3 mbar step	2.22	1.96–2.50	⋯	⋯	1.87	1.65–2.11[a]
Neptune	0.1 mbar step	7.55	6.65–8.50	⋯	⋯	2.02	1.78–2.28[b]
Neptune	0.01 mbar step	81.90	72.87–91.42	⋯	⋯	2.22	1.97–2.48[b]
Neptune	Moses & Poppe (2017)	⋯	⋯	0.63	0.55–0.70	1.88	1.66–2.11[a]
Neptune	**Combined H_2O column**	⋯	⋯	⋯	⋯	$\mathbf{1.9}^{+0.2}_{-0.3}$	

Notes. Uncertainty ranges include 1σ spectral fitting errors and uncertainty in temperature profile compiled from Table 2.
[a] Profiles provide adequate fit to measured spectra, are indistinguishable at 4σ significance, and are included in the combined H_2O column abundance figures in bold.
[b] Models give significantly worse fits than the best-fitting model and are not included in the combined H_2O column abundance figures.
[c] An SVP limit was not applied to these profiles.

by Moses & Poppe (2017). In addition, the total external oxygen flux would need to be closer to the upper bound of ablation model predictions, at around $\sim 2.5 \times 10^5$ cm^{-2} s^{-1}, in order to supply the necessary flux of H_2O to match our observations. (2) Ablation of IDP grains could supply H_2O and cometary impacts could supply CO via shock chemistry (Lellouch 1996; Cavalié et al. 2014; Moses & Poppe 2017; Lara et al. 2019). In this scenario IDPs could comprise mostly water ice, with a flux similar to that predicted by the Moses & Poppe (2017) ablation model and inferred from our observed H_2O abundance. CO_2 could be either supplied as a minor component in IDP grains or photochemically produced from H_2O following the schemes in Moses & Poppe (2017).

For Neptune, our observed external water flux of $12.7^{+1.3}_{-2.0} \times 10^4$ cm^{-2} s^{-1} is about six times less than the predicted oxygen atom flux of $7.5^{+16}_{-5.1} \times 10^5$ cm^{-2} s^{-1} from Moses & Poppe (2017). However, atmospheric processes on Neptune are more complex than on Uranus, so interpretation is not so straightforward. Neptune's warmer stratosphere means that the CH_4 homopause is much higher, with significant methane and associated photochemically produced hydrocarbons existing at pressures as low as $\sim 10^{-4}$ mbar (Moses & Poppe 2017). Therefore, unlike on Uranus, the pressure ranges where CH_4 and hydrocarbons exist overlap with the IDP ablation region, so photochemistry is more important in determining the form of oxygen. For example, hydrocarbons can convert H_2O into CO via photochemical reactions, but the effectiveness of this process is unclear, as significant abundances of CO can shield the UV radiation required to drive these photochemical reactions (Moses & Poppe 2017). The exact mechanism for ablation may also be important, with higher-temperature IDP ablation favoring production of CO over H_2O. If the photochemical schemes in Moses & Poppe (2017) accurately reproduce these processes in Neptune's atmosphere, then our observations suggest that IDP oxygen flux should be much lower, closer to the lower bound of the model prediction. However, if a larger fraction of supplied H_2O is converted to CO than is accounted for in the photochemical model, it is entirely possible that predicted total oxygen flux from the Moses & Poppe (2017) ablation model and inferred water flux from our observations could be consistent, especially if IDPs contain a significant CO component. The picture is also complicated by evidence of a recent large comet impact, supplying large amounts of CO into the stratosphere and mesosphere (Lellouch et al. 2005; Luszcz-Cook & de Pater 2013; Teanby et al. 2020). To fit Neptune's high stratospheric CO abundance ($\sim$1 ppm) requires a CO flux of $\sim 2 \times 10^8$ cm^{-2} s^{-1} (Moses & Poppe 2017). This is orders of magnitude larger than fluxes inferred by IDP ablation models (Poppe 2016; Moses & Poppe 2017) and the water abundance observed here ($\sim 10^5$ cm^{-2} s^{-1}). This supports the idea that a large comet impact is required to supply large amounts of CO into the stratosphere and mesosphere via shock chemistry (Lellouch 1996; Lellouch et al. 2005; Teanby et al. 2020).

Inferred external water fluxes from our observations are similar for Uranus ($8.3^{+4.0}_{-0.9} \times 10^4$ cm^{-2} s^{-1}) and Neptune ($12.7^{+1.3}_{-0.2} \times 10^4$ cm^{-2} s^{-1}). This implies that the approximately four times greater column abundance of water on Neptune is due to its warmer stratosphere allowing water to remain in vapor form, whereas the cold stratosphere on Uranus causes water vapor to condense out. This suggests that Uranus and Neptune may in fact have very similar IDP fluxes, unless there are significant water-loss processes that are not accounted for in current photochemical models (Moses & Poppe 2017; Lara et al. 2019). The dynamical model of Poppe (2016) predicts that the flux of IDP grains is around seven times higher on Neptune than on Uranus, but model uncertainties are large enough so as not to preclude a similar flux. The comet impact rates on Uranus and Neptune are also predicted to be quite similar (Levison et al. 2000; Zahnle et al. 2003), so both planets may experience similar external flux processes. This

suggests that we just happen to be observing Neptune at a time shortly after a large comet impact.

The 1994 SL9 Jupiter impact provides an interesting indicator of the effects a comet impact can have on giant planet stratospheric composition. Directly after the SL9 impact, many new stratospheric species were detected as a result of ablation, shock chemistry, and subsequent photochemical processing (Lellouch 1996; Moses 1996). In addition to providing large quantities of H_2O and CO, the impact produced NH_3, HCN, H_2S, S_2, CS, CS_2, and OCS (Lellouch et al. 1995; Noll et al. 1995; Lellouch 1996), although some of these species were very short-lived. Modeling of post-impact chemistry by Moses (1996) and follow-up observations (Moreno et al. 2003; Iino et al. 2016) suggest that CS, CS_2, and HCN are long-lived and can remain in the atmosphere for years. Therefore, these species could provide alternative diagnostics of past comet impacts. On Neptune both HCN and CS have been observed in the stratosphere (Marten et al. 1993; Lellouch et al. 1994; Rezac et al. 2014; Moreno et al. 2017). The CS observation requires shock chemistry and supports the large-comet-impact hypothesis (Moreno et al. 2017), but on Neptune HCN could have other production mechanisms involving a nitrogen source from Triton or dissociation of atmospheric N_2 by galactic cosmic rays (Lellouch et al. 1994). This complexity and range of processes involved highlights the importance of comparing chemical abundances on different planets for understanding atmospheric chemistry and external sources in the outer solar system.

6. Conclusion

Herschel-HIFI spectra at 557 GHz were used to determined stratospheric H_2O column abundances of $0.54^{+0.26}_{-0.06} \times 10^{14}$ cm^{-2} on Uranus and $1.9^{+0.2}_{-0.3} \times 10^{14}$ cm^{-2} on Neptune. Planetary rotation has a significant effect on observed emission-line shapes, and the disk-averaged nature of the observations required carefully accounting for.

For Uranus, cold stratospheric temperatures limit H_2O vapor to low pressures (<0.03 mbar), and observations can be well fitted with either scaled photochemical model profiles or uniform step-type profiles. For Neptune, H_2O is about four times as abundant, and warmer stratospheric temperatures allow water vapor to exist deeper in the atmosphere, potentially down to the ~1 mbar level. However, significantly improved spectral fits are obtained by scaling photochemical models or using uniform step-type profiles with a cutoff of ~0.3–0.6 mbar.

Observed abundances are compatible with previous water determinations from ISO-SWS (Feuchtgruber et al. 1997) and Herschel-PACS (Lellouch et al. 2010) but have increased precision due to the higher spectral resolution and signal-to-noise ratio of Herschel-HIFI.

Comparison of observed column abundances with model predictions (Moses & Poppe 2017; Lara et al. 2019) allows constraints to be placed on water flux due to IDPs. Rescaling the Moses & Poppe (2017) model profiles to match our observed column abundances suggests external water fluxes of $8.3^{+4.0}_{-0.9} \times 10^4$ cm^{-2} s^{-1} for Uranus and $12.7^{+1.3}_{-0.2} \times 10^4$ cm^{-2} s^{-1} for Neptune. Therefore, external water fluxes appear to be similar for both planets, assuming that photochemical models have captured all important water-loss processes. For Uranus, water flux is in reasonable agreement with IDP model predictions (Poppe 2016; Moses & Poppe 2017; Lara et al. 2019), although to simultaneously explain stratospheric CO with IDPs alone requires an oxygen flux at the upper end of predictions, with an icy component composed of ~1/3 water ice and ~2/3 CO ice. Alternatively, a cometary contribution could have supplied Uranus's stratospheric CO and IDPs could supply water. For Neptune, current IDP model predictions (Poppe 2016; Moses & Poppe 2017) of oxygen flux are a factor of about six times higher than our inferred external water flux, although atmospheric processing on Neptune is more complex and the fraction of water in IDPs is unknown. An additional external source from a large cometary impact is most likely required to explain Neptune's very high stratospheric CO abundance. For Neptune, it is not possible to draw any conclusions about possible H_2O/CO ratios in the icy component of IDPs, as the CO abundance is dominated by this large cometary source.

HIFI has been designed and built by a consortium of institutes and university departments from across Europe, Canada, and the United States under the leadership of SRON Netherlands Institute for Space Research, Groningen, The Netherlands, and with major contributions from Germany, France, and the United States. Consortium members are: Canada: CSA, U.Waterloo; France: CESR, LAB, LERMA, IRAM; Germany: KOSMA, MPIfR, MPS; Ireland, NUI Maynooth; Italy: ASI, IFSI-INAF, Osservatorio Astrofisico di Arcetri-INAF; Netherlands: SRON, TUD; Poland: CAMK, CBK; Spain: Observatorio Astronómico Nacional (IGN), Centro de Astrobiología (CSIC-INTA). Sweden: Chalmers University of Technology—MC2, RSS, & GARD; Onsala Space Observatory; Swedish National Space Board, Stockholm University—Stockholm Observatory; Switzerland: ETH Zurich, FHNW; USA: Caltech, JPL, NHSC. N.A.T., P.G.J.I., and M.S. were funded by the UK Science and Technology Facilities Council (STFC) and the UK Space Agency (UKSA). C.A.N. and M.A.C. were supported by the Fundamental Laboratory Research (FLaRe) Program at NASA GSFC for their effort in this work.

Facility: Herschel (HIFI).

Software: NEMESIS (Irwin et al. 2008) (https://github.com/nemesiscode/radtrancode), GMT (Wessel et al. 2013) (https://www.generic-mapping-tools.org).

ORCID iDs

N. A. Teanby https://orcid.org/0000-0003-3108-5775
P. G. J. Irwin https://orcid.org/0000-0002-6772-384X
M. Sylvestre https://orcid.org/0000-0001-7086-8882
C. A. Nixon https://orcid.org/0000-0001-9540-9121
M. A. Cordiner https://orcid.org/0000-0001-8233-2436

References

Atreya, S. K., Hofstadter, M. H., In, J. H., et al. 2020, SSRv, 216, 18
Borysow, A., & Frommhold, L. 1986, ApJ, 304, 849
Borysow, A., & Frommhold, L. 1987, ApJ, 318, 940
Borysow, J., Frommhold, L., & Birnbaum, G. 1988, ApJ, 326, 509
Broadfoot, A. L., Atreya, S. K., Bertaux, J. L., et al. 1989, Sci, 246, 1459
Cavalié, T., Hue, V., Hartogh, P., et al. 2019, A&A, 630, A87
Cavalié, T., Moreno, R., Lellouch, E., et al. 2014, A&A, 562, A33
Cavalié, T., Venot, O., Selsis, F., et al. 2017, Icar, 291, 1
Conrath, B. J., Gautier, D., Owen, T. C., & Samuelson, R. E. 1993, Icar, 101, 168
de Graauw, T., Helmich, F. P., Phillips, T. G., et al. 2010, A&A, 518, L6
Delahaye, T., Armante, R., Scott, N. A., et al. 2021, JMoSp, 380, 111510

Desch, M. D., Connerney, J. E. P., & Kaiser, M. L. 1986, Natur, 322, 42
Dick, M. J., Drouin, B. J., & Pearson, J. C. 2009, JQSRT, 110, 619
Feuchtgruber, H., Lellouch, E., de Graauw, T., et al. 1997, Natur, 389, 159
Fletcher, L. N., Drossart, P., Burgdorf, M., Orton, G. S., & Encrenaz, T. 2010, A&A, 514, A17
Fletcher, L. N., Gustafsson, M., & Orton, G. S. 2018, ApJS, 235, 24
Giorgini, J. D., Yeomans, D. K., Chamberlin, A. B., et al. 1996, AAS/DPS Meeting, 28, 25.04
Goody, R. M., & Yung, Y. L. 1989, Atmospheric Radiation: Theoretical Basis (2nd ed.; Oxford: Oxford Univ. Press)
Gubbins, D. 2004, Time Series Analysis and Inverse Theory for Geophysicists (Cambridge UK: Cambridge Univ. Press)
Hartogh, P., Lellouch, E., Crovisier, J., et al. 2009, P&SS, 57, 1596
Helled, R., Anderson, J. D., & Schubert, G. 2010, Icar, 210, 446
Herbert, F., Sandel, B. R., Yelle, R. V., et al. 1987, JGR, 92, 15093
Hesman, B. E., Davis, G. R., Matthews, H. E., & Orton, G. S. 2007, Icar, 186, 342
HIFI Observers' Manual 2011, HERSCHEL-HSC-DOC-0784, version 2.4, http://herschel.esac.esa.int/Docs/HIFI/pdf/hifi_om.pdf
Iino, T., Ohyama, H., Hirahara, Y., Takahashi, T., & Tsukagoshi, T. 2016, AJ, 152, 179
Irwin, P., Teanby, N., de Kok, R., et al. 2008, JQSRT, 109, 1136
Irwin, P. G. J. 2009, Giant Planets of Our Solar System: Atmospheres, Composition, and Structure (2nd ed.; Chichester: Springer-Praxis)
Jarchow, C., Hartogh, P., Lellouch, E., et al. 2010, AAS/DPS Meeting, 42, 11.26
Karkoschka, E. 2015, Icar, 250, 294
Kester, D., Avruch, I., & Teyssier, D. 2014, in AIP Conf. Ser. 1636, Bayesian Inference and Maximum Entropy Methods in Science and Engineering (Melville, NY: AIP), 62
Lara, L. M., Rodrigo, R., Moreno, R., & Lampón, M. 2019, A&A, 621, A129
Lellouch, E. 1996, in IAU Coll. 156, The Collision of Comet Shoemaker-Levy 9 and Jupiter, ed. K. S. Noll, H. A. Weaver, & P. D. Feldman (Cambridge: Cambridge Univ. Press), 213
Lellouch, E., Hartogh, P., Feuchtgruber, H., et al. 2010, A&A, 518, L152
Lellouch, E., Moreno, R., Orton, G. S., et al. 2015, A&A, 579, A121
Lellouch, E., Moreno, R., & Paubert, G. 2005, A&A, 430, L37
Lellouch, E., Paubert, G., Moreno, R., et al. 1995, Natur, 373, 592
Lellouch, E., Romani, P. N., & Rosenqvist, J. 1994, Icar, 108, 112
Levison, H. F., Duncan, M. J., Zahnle, K., Holman, M., & Dones, L. 2000, Icar, 143, 415
Lindal, G. F. 1992, AJ, 103, 967
Lindal, G. F., Lyons, J. R., Sweetnam, D. N., Eshleman, V. R., & Hinson, D. P. 1987, JGR, 92, 14987
Luszcz-Cook, S. H., & de Pater, I. 2013, Icar, 222, 379
Marten, A., Gautier, D., Owen, T., et al. 1993, ApJ, 406, 285
Melin, H., Stallard, T., Miller, S., et al. 2011, ApJ, 729, 134
Moreno, R., Lellouch, E., Cavalié, T., & Moullet, A. 2017, A&A, 608, L5
Moreno, R., Marten, A., Matthews, H. E., & Biraud, Y. 2003, P&SS, 51, 591
Moses, J. I. 1996, in IAU Coll. 156, The Collision of Comet Shoemaker-Levy 9 and Jupiter, ed. K. S. Noll, H. A. Weaver, & P. D. Feldman (Cambridge: Cambridge Univ. Press), 243
Moses, J. I., Cavalié, T., Fletcher, L. N., & Roman, M. T. 2020, RSPTA, 378, 20190477
Moses, J. I., & Poppe, A. R. 2017, Icar, 297, 33
Murphy, D. M., & Koop, T. 2005, QJRMS, 131, 1539
Noll, K. S., McGrath, M. A., Trafton, L. M., et al. 1995, Sci, 267, 1307
Orton, G. S., Moses, J. I., Fletcher, L. N., et al. 2014, Icar, 243, 471
Pilbratt, G. L., Riedinger, J. R., Passvogel, T., et al. 2010, A&A, 518, L1
Poppe, A. R. 2016, Icar, 264, 369
Press, W. H., Flannery, B. P., Teukolsky, S. A., & Vetterling, W. T. 1992, Numerical Recipes (2nd ed.; Cambridge UK: Cambridge Univ. Press)
Rezac, L., de Val-Borro, M., Hartogh, P., et al. 2014, A&A, 563, A4
Roelfsema, P. R., Helmich, F. P., Teyssier, D., et al. 2012, A&A, 537, A17
Shipman, R. F., Beaulieu, S. F., Teyssier, D., et al. 2017, A&A, 608, A49
Sromovsky, L. A., de Pater, I., Fry, P. M., Hammel, H. B., & Marcus, P. 2015, Icar, 258, 192
Sromovsky, L. A., Fry, P. M., & Kim, J. H. 2011, Icar, 215, 292
Sromovsky, L. A., Limaye, S. S., & Fry, P. M. 1993, Icar, 105, 110
Teanby, N., Irwin, P., Moses, J., & Helled, R. 2020, RSPTA, 378, 20190489
Teanby, N. A. 2009, C&G, 35, 566
Teanby, N. A., & Irwin, P. G. J. 2013, ApJL, 775, L49
Teanby, N. A., Irwin, P. G. J., & Moses, J. I. 2019, Icar, 319, 86
Teanby, N. A., Irwin, P. G. J., Nixon, C. A., et al. 2013, P&SS, 75, 136
Teanby, N. A., Showman, A. P., Fletcher, L. N., & Irwin, P. G. J. 2014, P&SS, 103, 250
Trafton, L., Melin, H., & Geballe, T. 2021, AAS/DPS Meeting, 53, 115.02
Warwick, J. W., Evans, D. R., Peltzer, G. R., et al. 1989, Sci, 246, 1498
Warwick, J. W., Evans, D. R., Romig, J. H., et al. 1986, Sci, 233, 102
Wessel, P., Smith, W. H. F., Scharroo, R., Luis, J., & Wobbe, F. 2013, EOSTr, 94, 409
Yelle, R. V., Herbert, F., Sandel, B. R., et al. 1993, Icar, 104, 38
Zahnle, K., Schenk, P., Levison, H., & Dones, L. 2003, Icar, 163, 263